SAND2015-2816C

Assessing Post-Ignition Pyrotechnic Behavior

Michelle N. Skaggs[1], Marcia A. Cooper[1], William W. Erikson[2]
[1]Explosive Technologies Group
[2]Engineering Sciences
Sandia National Laboratories, PO Box 5800 MS1452, Albuquerque, NM 87185
mnskagg@sandia.gov

Keywords: titanium, schlieren imaging, strand burner, combustion modeling

ABSTRACT

Pyrotechnic devices are useful for their multi-faceted performance capabilities. Assessment of the post-ignition behavior begins by studying the pyrotechnic within the device through burn rate experiments in a hybrid strand burner and development of a convective combustion model. It is noted through both burn rate studies that the pyrotechnic likely undergoes a steady-to-unsteady burning mode transition. This insight is discussed within the context of the multi-phase flow that exhausts into the surrounding device environment recorded in high-speed schlieren imaging. Evidence of strong shock motion, combustion gas expansion, and particle motion are presented.

1. INTRODUCTION

Pyrotechnic powders are used for a variety of applications that take advantage of the multiphase flow fields, the luminous high-temperature combustion plumes, and the rapid gas generation rates that are characteristics of pyrotechnic output. The constituents of a pyrotechnic mixture, including their relative amounts, constituent particle sizes, and powder bed density, directly influence the output characteristics. Depending on the application of the device in consideration, there are certain performance characteristics of interest. For instance, the flame spread rate and pressure time history, may be of prime importance to devices such as actuators, which drive pistons or perform other such mechanical work, whereas ignitors and initiators may be more concerned with particle sizes and temperatures of the combustion products.

Through a collaborative experimental and computational research effort, an assessment of the post-ignition behavior is presented for a pyrotechnic powder in the small geometries characteristic of pyrotechnic igniters and actuators. This work provides the first step towards developing a diagnostic tool able to study the entire functional lifecycle of a pyrotechnic part from electrical input to output characteristics (shock, gas, heat, light) useful for various applications.

The pyrotechnic powder of titanium subhydride potassium perchlorate ($TiH_{1.65}/KClO_4$, referred to as THKP) was studied in this work. The THKP powder is a 33% $TiH_{1.65}$: 67% $KClO_4$ mixture by weight with nominal particle sizes of 13 μm and 22 μm, respectively. The bulk powder density studied was a fraction of its theoretical maximum density ($\rho_{TMD} = 2.845$ g/cm^3), $\phi = \rho/\rho_{TMD}$.

The device under consideration in this work is a simple research igniter containing pressed THKP powder in a charge cavity with nominal dimensions of 0.221 cm in diameter and 0.191 cm in height for an aspect ratio of 0.86, shown in Figure 1. The top surface of the pressed powder remained open to the surrounding environment. Each research igniter was functioned by thermally heating a Tophet C bridgewire to ignite the pyrotechnic powder.

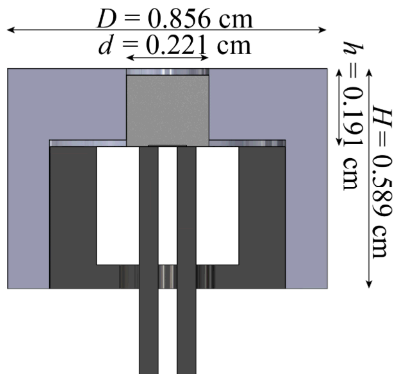

Figure 1. Illustrated dimensions of the cylindrical igniter body, D and H, and the charge cavity, d and h, for the research igniter

This paper contains the results of our three efforts categorized in terms of phenomena occurring within and external to the device: 1) application of traditional burn rate measurements to the smaller research igniter geometry; 2) presentation of an initial convective combustion model; and 3) schlieren images of the igniter output multiphase flow evolution within the surrounding environment.

2. COMBUSTION WITHIN DEVICE

2.1. Correlation of Burn Rate Experiments

The steady conductive burn rate of THKP ($\phi = 0.8$) has been previously measured in a hybrid strand burner and fitted to $r = BP^n$ with $B = 1.5054$ cm/s MPa^{-n} and $n = 0.5239$ [1]. In the large ullage of the strand burner vessel, initially filled with argon, the pressure rise during strand combustion is relatively modest. For a strand with nominal diameter of 6.35 mm, the pressure raised 1.2 MPa after consuming 2.54 cm of the strand. After which, the combustion mode was observed to transition from a steady conductive mode to a deconsolidated burning mode that rapidly consumed the remaining material. This steady-to-unsteady burning mode transition was observed over a range of initial densities and initial pressures.

As an initial attempt to relate the strand-burner-measured burn rates to the much smaller igniter scale, the previously derived universal relationship [1] between pressure and amount of strand consumed is utilized. This relationship describes the dependence of the pressure rise ($P-P_0$) in the free volume of the vessel V_{u0} on the gas-phase products generated by combustion (with burn surface area S_x) of the initial solid material (with density ρ). Thus, reduced parameters of Π and χ include the solid material density and vessel ullage respectively [1]:

$$\Pi = \frac{P-P_0}{\rho} \qquad \chi = \frac{S_x}{V_{u0}} x$$

$$\Pi = \frac{\chi}{1+\chi}$$

Utilizing this relationship for analysis of the research igniter considered here (Figure 1) requires that several assumptions, made in the application of this relationship to the strand burner facility, remain valid at this smaller length scale. These include: 1) a constant co-volume approximation of $1/\rho_s$ despite the near-zero ullage; 2) an unvarying burn surface area; and 3) the steady rate burn law is valid throughout entire range of pressures. Evaluating the validity of these assumptions with scale is the subject of ongoing investigations.

Nonetheless, applying the universal relationship to the research igniter predicts a rapid pressure rise within the charge cavity as shown in Figure 2. Different assumptions of the burn surface area S_x are also plotted [1]. It was previously shown that $S_x = 0.6V_0/L$ best represented the burn surface area in the strand burner experiments.

Shown on Figure 2 is the critical pressure at which transition to deconsolidated burn is expected [1]. It is clear that this occurs early in time and after only a small fraction x/L of the pellet has been consumed. These experiments form the motivation for developing predictive model capabilities to capture these basic combustion phenomena across scales.

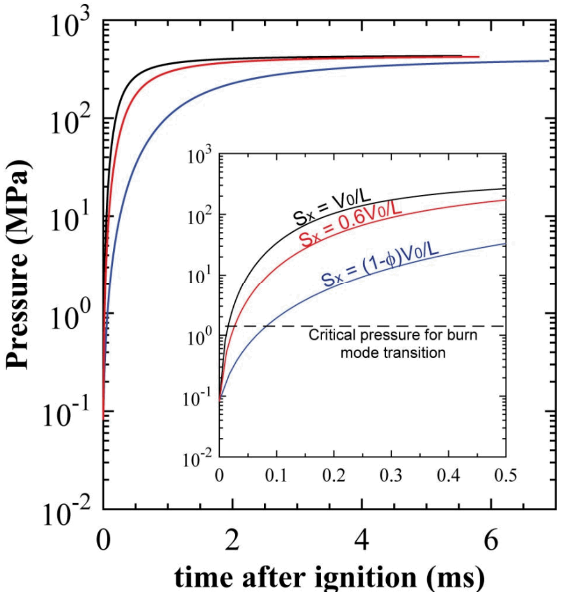

Figure 2. Predicted pressure using universal relationship derived in [1] for length scales of research igniter. Early transition to deconsolidated burn is predicted. Combustion Model Development

The simple convective combustion model can be described as a model for solid particle combustion coupled with a porous flow model for gas transport. In essence, burning particles produce high temperature gas which then flows to adjacent particles, heating them up. Upon reaching a threshold ignition temperature (T_{ign}), those particles also ignite, combust, and release hot gases thereby further propagating the reaction. In keeping with our keep-it-simple philosophy, the particles are treated as shrinking spheres with uniform initial size and the gas transport is done via a Forchheimer-corrected Darcy's law. Simple gas phase equations of state (ideal gas or Noble-Abel) are used. For now we have neglected particle bed compaction and certain flow effects (turbulence, supersonic flow, etc.).

The shrinking sphere burning model can be cast into a form based on the volumetric extent of reaction, α, defined as $\alpha = 1 - V/V_0$ where V_0 is the original particle volume. The volumetric burning rate of a particle is given by:

$$\frac{dV}{dt} = 4\pi(1-\alpha)^{2/3} r_{burn}$$

where r_{burn} is the particle burning rate (length/time) and can be a constant or an exponential function of pressure (i.e. $r_{burn} = BP^n$, where n may be zero). In practice, the multiplicative constants are lumped together and we define the mass burning rate (kg/m^3-s) of a collection of particles at a given location as:

$$\dot{\omega}'''_{rxn} = A\rho_s(1-\alpha)^{2/3}P^n$$

We allow a certain fraction of the reactant material to form gaseous products, while the remainder is in the solid phase. Energy is also released during this process. This is summarized by:

$$\text{Reactant} \rightarrow F_g\,\text{Gas} + (1-F_g)\,\text{Solid} + \Delta H_{rxn}$$

In the above expression, F_g represents the mass fraction of the reactant that forms gases and ΔH_{rxn} is the energy release (mass basis). Naturally, some of this released energy will go with the gas products while the rest will remain with the solid products. We will call the fraction of ΔH_{rxn} which goes with the gas f_g; the portion remaining with the solid products is $(1-f_g)$. It is possible but perhaps not required that the energy apportionment to the gas phase, f_g, is equal to the mass apportionment, F_g.

The energy equations used in this work consist of two separate contributions: a solid phase equation associated with the particle bed, which includes thermal conduction and a gas phase equation, which includes diffusion and advection. Two separate phase temperatures are tracked and heat transfer between the two phases is computed via a heat transfer coefficient. There is also a source term associated with the heat of reaction. The pressure-volume work term is also included.

The governing equations for the solid and gas phase regions are given here:

Mass conservation (solid & gas phases):

$$\frac{\partial \rho_s'}{\partial t} = -\dot{\omega}_{rxn}''' F_g$$

$$\frac{\partial \rho_g'}{\partial t} + \nabla\cdot(\rho_g' \mathbf{v}) = \dot{\omega}_{rxn}''' F_g$$

Energy equations (solid & gas phases):

$$\frac{\partial(\rho_s' C_{p,s} T_s)}{\partial t} = \lambda \nabla^2 T_s + h_v\left(T_g - T_s\right) + \dot{\omega}_{rxn}''' \Delta H_{rxn}\left(1 - f_g\right)$$

$$\frac{\partial(\rho_g' C_{p,g} T_g)}{\partial t} + \nabla\cdot(\rho_g' \mathbf{v} C_{p,g} T_g) = \nabla\cdot(\rho_g' D C_{p,g} \nabla T)$$

$$+ \frac{\partial(\theta P)}{\partial t} + h_v\left(T_g - T_s\right) + \dot{\omega}_{rxn}''' \Delta H_{rxn} f_g$$

Note the inclusion of the terms for advection (second term on left hand side) and gas diffusion (first term on right hand side) of the gas energy equation. Thermal conduction in gas phase has been neglected here. The primed densities represent bulk quantities in terms of porosity, θ, and the material densities: $\rho_g' = \theta \rho_g$ *and* $\rho_s' = (1-\theta)\rho_s$.

For this initial version, in lieu of true full momentum equations for the two phases, we have used a simplified approach. For the solid phase, we assume the particles remain fixed. For the gas phase, the pressure-velocity relationship for the porous flow is given by the following equation where the first term on the right hand side is the standard Darcy's law form and the second is the Forchheimer term to correct for inertia.

$$-\nabla P = \frac{\mu}{k}\mathbf{v} + \rho\beta|\mathbf{v}|\mathbf{v}$$

In the above, $\mathbf{v}$ is the velocity vector, μ is viscosity, k is permeability, ρ is density, and β is an effective inertia coefficient (here β chosen as 0.55 m^{-1}).

The permeability, k, is treated as a power law function of the porosity, θ, and is based on measurements of pyrotechnic materials as shown in Figure 3 [2,3].

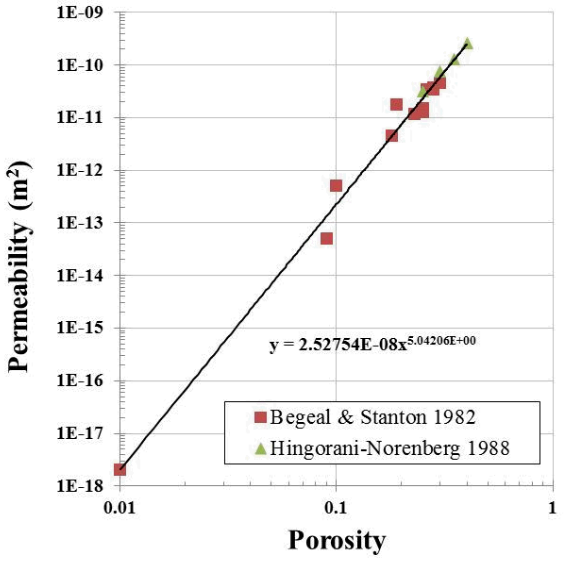

Figure 3. Permeability as a function of porosity for pyrotechnic materials, from Refs. 2 and 3.

The heat of reaction, average heat capacity, gas molecular weight and product gas fraction were obtained from constant volume explosion computations [4] for THKP taken at low density. The baseline values used in the model are: C_p = 850 J/kg-K, W = 39 g/mol, ΔH_{rxn} = -3.8e7 J/kg, F_g = 0.5 (at higher pressures/densities the molecular weight and gas fraction change substantially, we have not accounted for that effect here). Values of transport coefficients were taken as D = 2e-5 m^2/s and λ = 1 W/m-K. A volumetric heat transfer coefficient, h_v (standard heat transfer coefficient multiplied by the particle's surface-to-volume ratio) of 1e9 W/m^3-K was used. A temperature-dependent viscosity was used (2e-5 to 1.2e-4 N-s/m^2 from 300 to 5000 K), estimated from air properties.

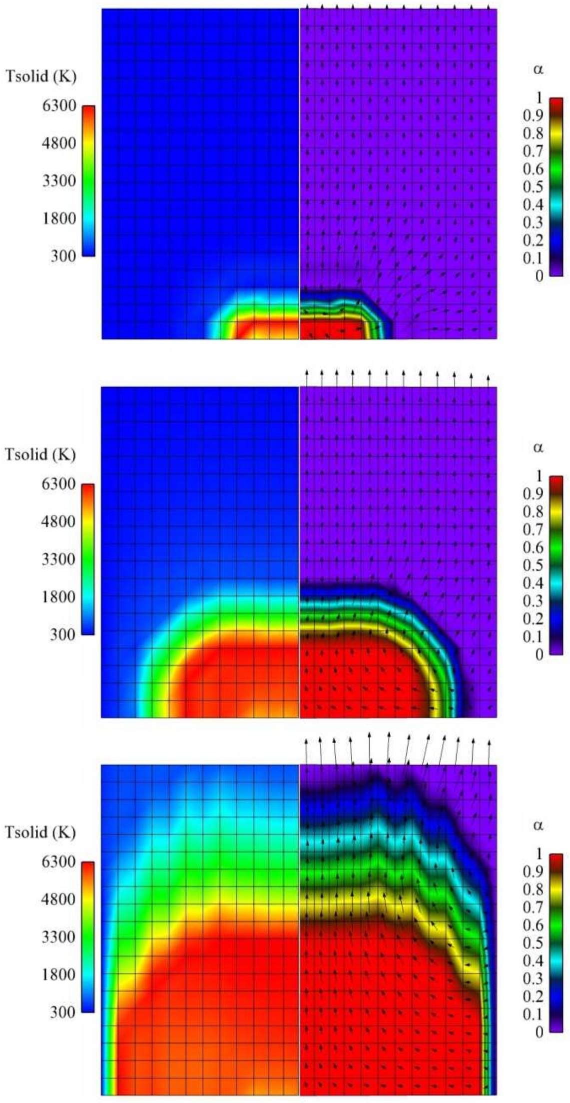

Figure 4. Baseline 2-D axisymmetric simulation results showing solid temperature (left) and extent of reaction/velocity vectors (right) at three times after ignition: top=0.5 ms, middle=1.0 ms, bottom=1.35 ms.

Simulations were performed using the finite element model described above. Figure 4 shows the solid temperature and the extent of reaction profiles at three different times. The velocity vectors are also given. The color bands for α, give an indication of the ignition front location (purple/dark blue interface) and burnout location (yellow/red interface). Note that the flame zone is rather thin early in time, but spreads out as the hot gases quickly spread through the domain and ignite particles.

It is also interesting to note that early in the burn, the gas velocity is essentially normal to the burn front (i.e. the gases flow exclusively outward away from the burning). At later stages, the flow direction changes over part of the domain near the outer edge (a wall location) such that the gases generated flow back through the already burned material. This is because the permeability has increased in the already burned region allowing gases to more easily flow that direction toward the exit at the top, instead of through the unburned material near the wall. This results in a slowdown of the ignition front propagation near the side wall.

There are also mesh-dependent instabilities in the combustion which appear as wavy patterns in the extent of reaction. We have not as yet fully resolved all the phenomena, nor have we fully established the best set of model parameters to represent the situation at hand, so these results must be considered as preliminary. That said, several different runs were performed in order to elucidate the effects of various model parameters. In particular, we have looked at three: the solid particle ignition temperature (T_{ign}), the particle burning rate coefficient (A) and the volumetric heat transfer coefficient (h_v).

It can be argued that an appropriate ignition temperature is the melting point of $KClO_4$ of 610°C (883 K) since oxygen for combustion must arise from decomposition of that material, and decomposition rates dramatically increase upon $KClO_4$ liquefaction [5, 6]. Hence for our baseline calculation we used 883 K as a particle ignition temperature. One-off calculations in which the ignition temperature was assumed to be 50 K higher or lower were also performed. The baseline value for A and h_v were arbitrarily chosen at 5000 1/s and 10^9 W/m^3-K. The effects of these two parameters were also investigated by varying them by ± 20% of their baseline values.

Figure 5 shows the relative effects on the overall integrated extent of reaction. As expected, increasing the ignition temperature leads to a slower reaction rate, while lowering it speeds things up. Increases in A and h_v both led to faster reaction rates, while decreases slowed the process. Relatively speaking, the combustion process is less sensitive to changes in h_v than in the reaction rate constant, A.

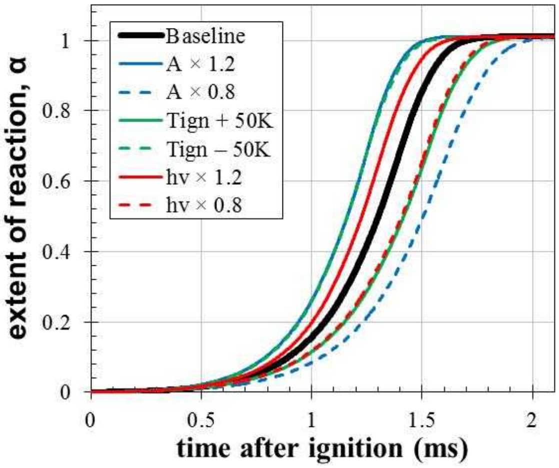

Figure 5. Overall reaction rate for combustion simulations of baseline and one-off cases showing sensitivity effects of reaction rate (A), particle ignition temperature (T_{ign}) and solid-gas heat transfer coefficient (h).

One of the principal desired outputs is information on the gases produced by the pyrotechnic material. Figure 6 shows the gas temperature and the mass flux (per unit area).

Another variable of interest is the pressure produced by the combustion process. Figure 7 shows the spatial profiles at the same points in time as the snapshots in Figure 4 for the baseline case.

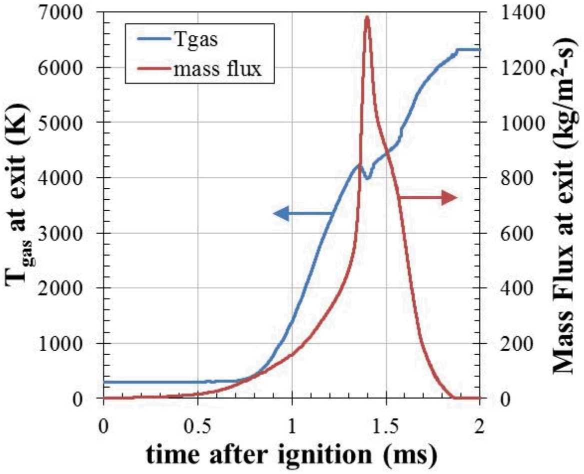

Figure 6. Gas temperature and mass flux at exit location from baseline simulation.

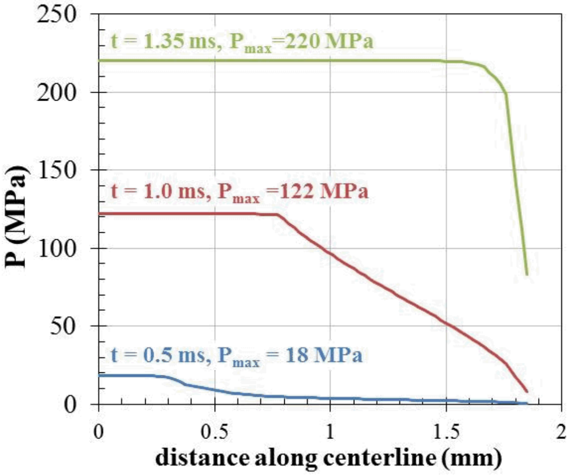

Figure 7. Pressure distribution along centerline at times corresponding to the snapshots in Figure 4.

Note that the pressure profiles in Figure 7 behind the reaction front are fairly flat (associated with increasing permeability) but ahead of the front the pressure gradients become steeper with time. The simplistic form of the model used here is not sufficient to capture shock formation, material compaction and other phenomena which may be of interest; that would require a more complete multi-phase momentum description. Nevertheless, the current result that hundreds of MPa of pressure have evolved well before the burn front reaches the exit location indicates more than sufficient pressure to generate a shock wave once that gas does break out. Where and when that breakout will occur will depend on material strength (including inertial strength) of the compacted pyrotechnic material.

3. MULTIPHASE FLOW EXTERNAL TO DEVICE

3.1. High-speed schlieren imaging

A schlieren imaging system (Figure 8) was designed [7] for use with pyrotechnic igniters known to have intense self-illumination and relatively long duration reactions. A Specialized Imaging SILUX640 laser light source provided non-coherent illumination centered at 644 nm with an 8-nm-wide bandwidth. In combination with a laser line filter centered at 640 nm with a 12-nm-wide notch, the pyrotechnic self-light was filtered allowing for visualization of the blast wave, particle motion, and expanding combustion gas volume from the pyrotechnic igniter. A Shimadzu HPV-2 high-speed camera captured 102-frame image sequences of the pyrotechnic event at 500 kHz and 250 ns exposure. The camera CCD was 2.07 cm wide × 1.72 cm tall with pixel sizes of 66.3 µm × 66.3 µm for a total of 312 × 260 pixels in each image.

Optics were selected to capture a field of view at least 8 cm above the research igniter. The collimating and schlieren lenses were two 15.24-cm-diameter plano-convex achromatic lenses. The cutoff (a vertically-oriented razor blade) was placed at the focal point of the schlieren lens and inserted into the beam to block approximately two-thirds of the beam spot. The laser line filter and a 2.0 neutral density filter were placed after the cutoff. Finally, a combination of biconvex lenses was used to demagnify the image at the object plane of the schlieren lens onto the CCD of the camera.

The experimental timing was fixed by the triggering sequence required to couple the firing signal from the laser diode driver (LDD), the limited laser pulses, and the 102-frame camera recording length. The SILUX640 laser system has a maximum run time of 30 µs, which was split into 120 discrete pulses, each of 250 ns duration at a frequency of 500 kHz to match the camera frame rate. This triggering configuration did not allow for imaging of the pyrotechnic event at or near breakout (seen in Figure 9).

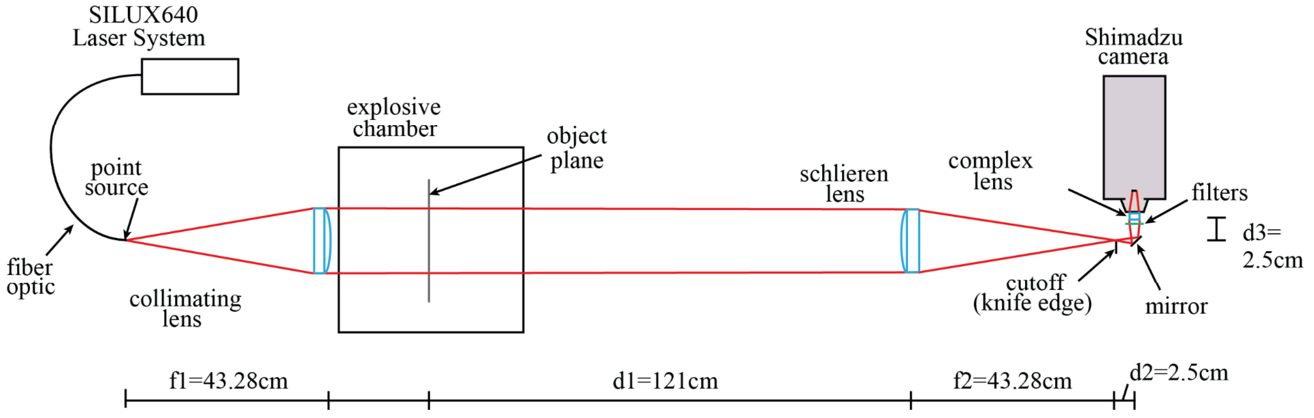

Figure 8. Schlieren imaging system designed for imaging of pyrotechnic events. SILUX640 laser system provides effectively non-coherent illumination. Shimadzu camera records 102-frame image sequences with 312×260 pixels. Field of view of system captures 8 cm radius from igniter.

3.2. Images of multiphase flow

In each test, 102-frame image sequences were captured of the post-ignition behavior of the pyrotechnic igniters. The open top charge cavity of the igniter is located near the bottom right corner in the images. A portion of the image sequence (nominally 50-80 frames) captured the roughly hemispherical blast wave propagation across the field of view. The optically dense multiphase volume of gaseous combustion products and unburned particle cloud propagate behind the blast wave. Images have been presented for a THKP test ($\phi = 0.76$) in Figure 9.

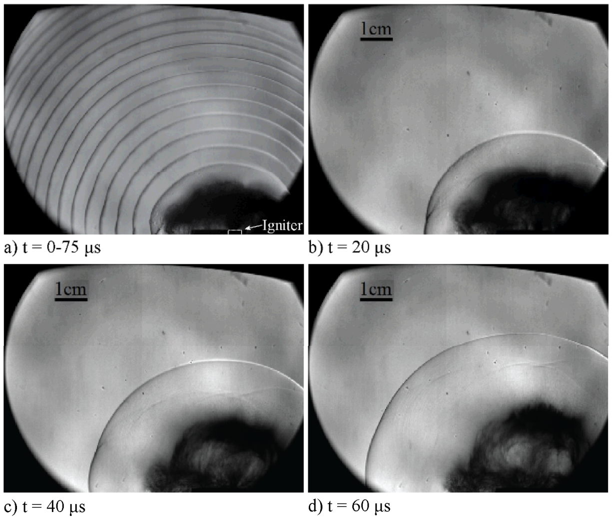

a) t = 0-75 μs
b) t = 20 μs
c) t = 40 μs
d) t = 60 μs

Figure 9. Four frames are shown from a THKP test (ϕ=0.76). The first composite frame shows the blast wave shape evolution in time, shown every 10 μs until no longer visible in the field of view. The subsequent three frames are 20 μs apart, showing the gas volume expansion and particle motion. Gamma correction has been applied to all frames to enhance features.

Multiphase combustion products and particle motion are seen in Figure 9b-d behind the shock wave. Presumably unburned, solid particle fields were observed in all tests done with THKP, qualitatively suggesting that the combustion reaction did not consume all of the pyrotechnic powder in the charge cavity. Figure 10 shows a single cropped frame from three individual THKP tests repeating the same test conditions (ϕ = 0.76) and configuration.

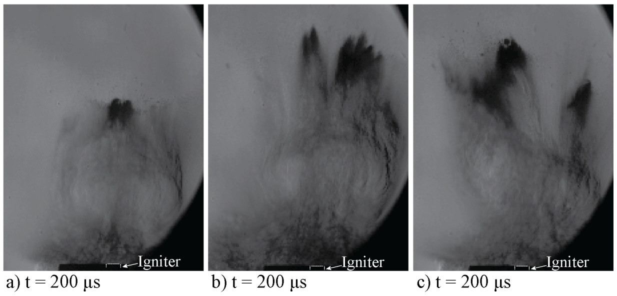

a) t = 200 μs
b) t = 200 μs
c) t = 200 μs

Figure 10. Evidence of unburned solid particles are shown for several THKP tests, each at 200 μs.

In all three tests, the opaque region of the image is presumed to contain unburned pyrotechnic powder that has been ejected from the charge cavity. Resolving individual particle sizes at this magnification and resolution was not feasible. In the future, increased magnification or resolution and other optical techniques will be employed to resolve particle size and quantity, then infer the mass of the unburned powder to make conclusions about the percentage of the pyrotechnic powder contributing to output from the device.

3.3. Analysis of shock motion

The characteristic radius-versus-time data points from the test shown in Figure 9 were identified through a process of edge tracking the shock wave followed by a statistical representation of the probability distribution function of radius across all angles about the axis of the igniter [8]. Then, the data points were fitted to the Dewey [9] blast wave equation:

$$R = A + Ba_0t + C\ln(1 + a_0t) + D\sqrt{\ln(1 + a_0t)}$$

where R is the shock radius, t is time, A-D are fitted coefficients, and a_0 is the sound speed of the air at absolute temperature. B is set equal to one to ensure that the shock speed approaches sonic conditions at late time. Figure 11 shows the individual data points and the blast equation curve fit to those points. The uncertainty analysis for this test can be found in Ref. 7.

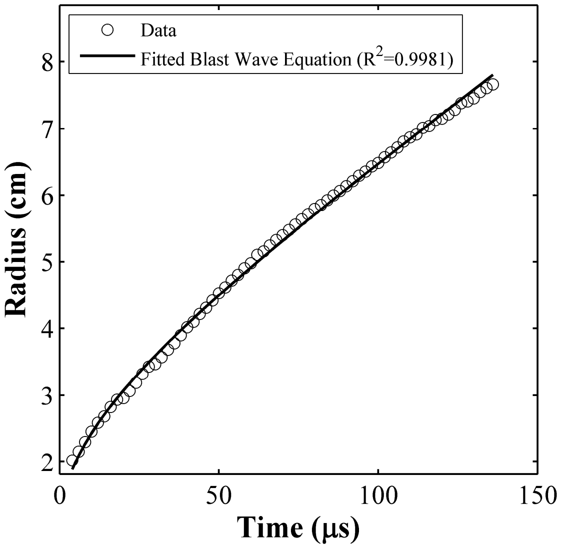

Figure 11. Plot of characteristic radius versus time for the THKP igniter test shown in Figure 9. Data points are shown as circles while the blast wave curve fit is shown as the solid line.

The blast wave was tracked for nearly 8 cm and 136 μs. The blast wave had sufficient strength to remain visible within the entire field of view. Strong agreement of the curve fit to the data appears in Figure 11.

Each radius-versus-time data point was converted to a blast pressure-versus-characteristic radius point using the following three equations for shock speed, Mach number, and blast pressure.

$$U = \frac{dR}{dt} \qquad M = \frac{U}{a_0}$$

$$\Delta P = P_S - P_0 = \frac{2\gamma P_0}{\gamma + 1}(M^2 - 1)$$

The blast pressure-versus-characteristic radius points and the representation of the blast curve fit in terms of blast pressure-versus-characteristic radius are shown in Figure 12.

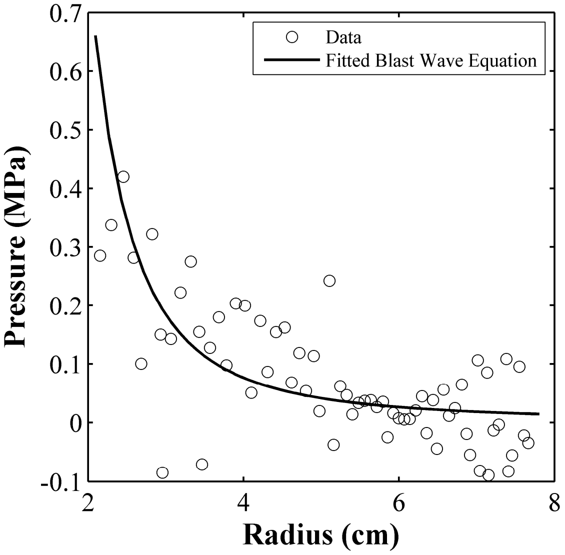

Figure 12. Plot of blast pressure versus characteristic radius for the THKP igniter test shown in Figure 9. Data points are shown as circles while the blast wave curve fit is shown as the solid line.

The pointwise differentiation used to find the shock speed of the data and then subsequently calculate Mach number and pressure ratio increases the observed scatter in the data shown in Figure 12. However, the blast wave decay of the pressure is evident. The pressure values around characteristic radius values of 2-3 cm correspond to a 2-2.3 Mach shock wave. The pressure decays to nearly ambient conditions within the field of view.

4. DISCUSSION

The pressure data correlate well between the studies within the device, but does not converge with the data measured externally to the device. The burn rate data predicts that the pressure is over 100 MPa at 1 ms after the time of ignition. The combustion model predicts that the pressure at 1.35 ms and only half the height of the charge cavity is over 220 MPa, which agrees reasonably with the burn rate data. In contrast, the pressure predicted by the imaging results is only nominally 0.4 MPa at breakout, when the camera system is triggered to record images of the pyrotechnic event at nominally 2 ms after start of current in each test. However, the lack of near-field, early-time data in these shots, due to the triggering sequence required to synchronize the camera, laser pulses, and firing signal as discussed above, hinder direct comparison.

There is strong correlation across all research efforts that the pyrotechnic material is not completely consumed by the combustion reaction within the charge cavity. The evidence of unburned particles in the imaging results support the predictions of the transition to deconsolidating burning from both the burn rate data and the combustion model.

5. CONCLUSIONS

We present the results from three efforts aimed at improved understanding of pyrotechnic device behavior including the combustion phenomena within the device to the resulting output multiphase flow within the environment surrounding the device. Each effort considered THKP at nominally ϕ = 0.80 in a common research igniter geometry. Consistent phenomena of the generation of large pressures from conductive combustion suitable for the production of strong shock waves in the surrounding environment, the likelihood of steady-to-unsteady combustion mode transition within the charge cavity of the device and ejection of solid, unburned particles are suggested from these three experimental and computational research efforts. A number of areas of future work have been identified in order to improve the understanding of pyrotechnic device performance and the interplay of combustion performance to output.

ACKNOWLEDGEMENTS

The authors would like to thank Michael Oliver, Ian Kohl, Ryan Marinis, Duane Richardson, and Cody Love for assisting with various aspects of both experimental efforts. We appreciate the efforts of David Glaze, Steve Kennon, Mario Martinez, Sam Subia, and Lindsey Erickson for assistance in developing the porous flow combustion model.

Sandia is a multi-program laboratory operated by Sandia Corporation, a Lockheed Martin company, for the United States Department of Energy's National Nuclear Security Administration under contract No. DE-AC04-94AL85000. Approved for public release, SAND2014-XXXXC.

REFERENCES

---

[1] Cooper, M.A., & Oliver, M.S. (2013). The Burning Regimes and Conductive Burn Rates of Titanium Subhydride Potassium Perchlorate ($TiH_{1.65}/KClO_4$) in Hybrid Closed Bomb-Strand Burner Experiments, *Comb. and Flame*, **160**, 2619-2630.

[2] Begeal, D.R. & Stanton, P.L. (1982). Pyrotechnic Deflagration Velocity and Permeability, *8th International Pyrotechnics Seminar*, 112-128.

[3] Hingorani-Norenberg, S.L.R. (1988). An Experimental Study of the Burn Rate of $TiH_{1.65}/KClO_4$ Pyrotechnic Under Confinement, Sandia National Laboratories Report, SAND88-2393.

[4] Hobbs, M.L., Brundage, A.L., & Yarrington, C.D. (2014). JCZS2i: An Improved JCZ Database for EOS Calculations at High Temperature and Pressure, *15th International Detonation Symposium*, San Francisco, CA.

[5] Harvey, A.E. et al. (1954). The Kinetics of the Isothermal Decomposition of Potassium Perchlorate, *J. Amer. Chem. Soc.,* **76**, 3270-3273.

[6] Harvey, A.E. et al. (1960). Isothermal and Isopiestic Decomposition of Potassium Perchlorate and Potassium Chlorate, *Annals of the New York Academy of Sciences*, **79**(11), 971-987.

[7] Skaggs, M.N. (2014). Characterization of Pyrotechnic Igniter Output with High-Speed

---

Schlieren Imaging, (Master's thesis), New Mexico Institute of Mining and Technology, Socorro, NM.

[8] Skaggs, M.N., Kohl, I.T., Hargather, M.J., & Cooper, M.A. (2015) Characterizing Pyrotechnic Igniter Output with High-Speed Schlieren Imaging. *Comb. and Flame*. In Review.

[9] Dewey, J.M. (1989). *Handbook of Flow Visualization*. 3rd Edition. Hemisphere Publishing Corporation.